Progress In Electromagnetics Research, Vol. 184, 64–78, 2025 PIER

(Received 22 October 2025, Accepted 5 December 2025, Scheduled 20 December 2025)

A Random Phase Approximation Method for the Generation of Complex Beams and Its Verification via Phase-Only Digital Metasurfaces

Caiyu Qian[1, †], Zhenjie Qi[1, †], Zhengxing Wang[2], Hui Xu[1], Xuanjing Li[1], Ruiwen Shao[1], Junwei Zhang[1],
Lingang Fan[3], Youjia Chen[4], Zhangjie Luo[1], Junyan Dai[1], Junwei Wu[1, *], Qiang Cheng[1], and Tiejun Cui[1]

[1] *The State Key Laboratory of Millimeter Waves, Southeast University, Nanjing 210096, China*
[2] *The State Key Laboratory of Terahertz and Millimeter Waves, City University of Hong Kong, Hong Kong 999077, China*
[3] *The National Key Laboratory of Space Target Awareness, Beijing Institute of Radio Measurement, Beijing 100854, China*
[4] *The College of Physics and Information Engineering, Fuzhou University, Fuzhou 350108, China*

ABSTRACT: Complex beams hold significant value in radar and communication systems due to their distinctive propagation characteristics. Digital metasurfaces, which can dynamically control electromagnetic (EM) waves, play an important role in realizing complex beams. Conventional analytic and optimization methods face challenges in synthesizing complex beams of low-bit digital metasurfaces due to the quantization error and the high computational complexity. Here, we propose a statistical method to realize complex beams with phase-only digital metasurfaces. To this end, we introduce tailored quantization probabilities to design the discrete random phase distributions, which approximate the continuous excitation coefficients derived from analytic methods. Based on the proposed method, we analyze the error between the realized and target patterns. These findings offer critical insights into the accuracy of random quantization. Complex patterns with cosecant, prescribed null, flat-top, and dual-beam are designed and validated in combination with a 2-bit phase coding digital metasurface. The experimental results are in good agreement with the theoretical analysis. This work pioneers the application of random phase approximation and statistical synthesis in digital metasurfaces, providing a fast and efficient route for realizing complex beams in modern radar and wireless communication technologies.

1. INTRODUCTION

Complex beams have extensive applications in various fields such as radar, sensing, and wireless communications. For example, flat-top beam antennas provide a stable gain within a given angular range and maintain low side-lobe levels outside the region [1–3]. Cosecant beam antennas compensate for propagation losses over varying distances [4, 5]. Null steering antennas maximize signal power in the direction of the intended receiver, while reducing the power in the directions of potential eavesdroppers [6–8].

Realizing complex beams by traditional antenna arrays results in additional feed network. Moreover, the antenna element exhibits complicated structures for better performance [9]. Metasurfaces consisting of subwavelength metallic or dielectric elements have opened up unprecedented possibilities for EM wave manipulation [10, 11]. Digital metasurfaces, proposed by Cui et al. [12], have been widely investigated in recent years. They can flexibly control EM waves with a finite number of elements in a discretized manner, offering simplified designs and various functions in programmable ways [13–22]. In particular, complex beams can be effectively realized by digital metasurfaces [23, 24].

The key point in realizing complex beams based on digital metasurfaces is designing the amplitude and phase distributions of the array. Historically, a variety of methods have been proposed for traditional array beamforming, which serve as valuable references. Analytic methods such as Fourier transform [25–28], Schelkunoff [29, 30], and Woodward-Lawson synthesis [31–33] are used to realize complex beams with continuous amplitude and phase distributions for an equispaced array. Additionally, the phase distribution can be compensated to realize complex beams without amplitude control [34]. Although these analytic methods do not achieve the best performance, they provide sub-optimal solutions with continuous excitation coefficients immediately. It is noted that digital metasurfaces only offer a limited number of discrete amplitude and phase responses. Direct quantization of the continuous excitation coefficients will inevitably bring errors. Moreover, the implementation of amplitude modulation in most analytic methods requires a complicated design of metasurface elements with energy loss.

Stochastic optimization methods like ant colony [35, 36], simulated annealing [37, 38], particle swarm [39], and genetic algorithm [40–43] have been used widely in designing radiation patterns with low side lobe levels. In principle, these methods can be tailored to obtain the discrete phase distributions of digital metasurfaces. Nevertheless, they always require ex-

---

[*] Corresponding author: Junwei Wu (jwwu@seu.edu.cn).
[†] These authors contributed equally to this work.

doi:10.2528/PIER25102203 Published by THE ELECTROMAGNETIC ACADEMY

tensive computation, and the optimization time increases significantly for metasurfaces with massive elements. In the last few years, several methods have been proposed to improve the computational efficiency, including adaptive genetic [44] and multiobjective particle swarm [45]. However, it is non-trivial to achieve an optimal balance between performance and computation time.

It is noted that the continuous excitation coefficients derived from analytic methods can be discretized to realize rapid synthesis. Random quantization, which approximates the continuous amplitude and phase by discrete quantities with a specific random function, had been investigated in combination with antenna array design [46–48]. The two probable values (2PV) and three probable values (3PV) methods in [46] aim to statistically reduce the phase quantization errors, thereby mitigating the beam pointing deviation and side lobe level. Unlike the 2PV and 3PV methods, which only focus on the phase of each element, the four probable values (4PV) method proposed by Kashin in 1971 [49] approximates the amplitude of each element with random phase distributions. Simulations demonstrate that the 4PV method achieves effective amplitude tapering, expanding the applications of random quantization methods for far-field pattern synthesis. However, the 4PV method does not achieve the simultaneous approximation of the continuous amplitude and phase distributions of elements. Although the above methods remain theoretical and are numerical investigations, they motivate this study to explore the realization of complex beams with random phase approximation.

In this paper, a novel statistical synthesis method is first introduced to design the coding distribution of phase-only digital metasurfaces, with a conceptual sketch shown in Fig. 1. Unlike [49], this work approximates the continuous amplitude and phase simultaneously with the discrete random phase, providing improved beamforming performance of digital metasurfaces. In light of the randomness of the proposed method, we provide the optimization process employed to obtain the optimal result, which has guiding significance for the study of random phase approximation.

The proposed method allows the continuous excitation coefficients derived from conventional analytic synthesis methods to be achieved using phase-only digital metasurfaces with discrete states. It is also noted that the low computational complexity of the proposed method facilitates its implementation in embedded systems. Numerical examples and full-wave simulations are presented to demonstrate the effectiveness of the proposed method. As an example, a 2-bit phase-only digital metasurface is utilized to realize complex beams through experimental measurements. The results are in good agreement with the simulations. This work transforms the statistical method in [49] from a mere numerical result to a practical route with a new lease of life in digital metasurfaces.

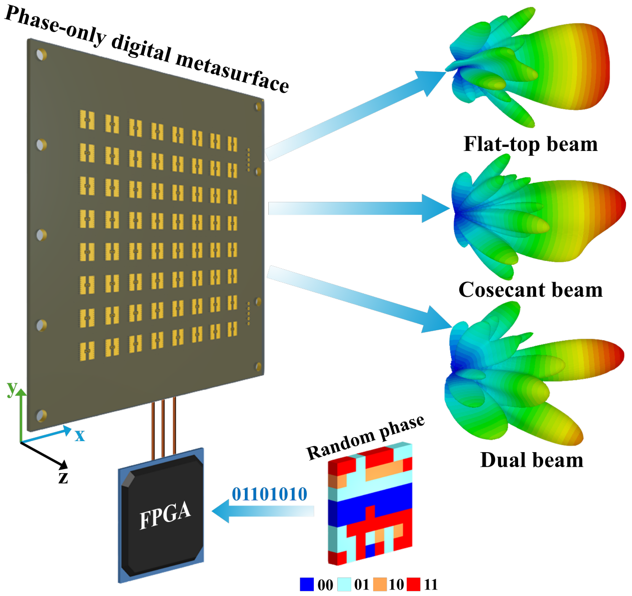

FIGURE 1. The schematic diagram of various complex beams generated by the phase-only digital metasurface.

2. METHODS

2.1. Derivation of the Method

The continuous amplitude and phase distributions of the digital metasurface are initially given by appropriate analytic synthesis methods. The discrete phases of each metasurface element are then determined based on specific quantization probabilities. The schematic workflow of the proposed method is shown in Fig. 2. The target pattern is a cosecant beam. Specifically, the beam varies between $\theta = 8^\circ$ and $\theta = 20^\circ$ in the $\phi = 0^\circ$ plane. To simplify the introduction, a uniform planar array (UPA) with a continuous amplitude and phase distribution is chosen as an example. If the reference point is taken at the center of the first element, the radiation pattern is expressed as follows:

$$F(\theta,\phi) = \sum_{m=1}^{M}\sum_{n=1}^{N} A_{mn} \cdot e^{j\varphi(m,n)} \cdot e^{j(kx_{mn}u+ky_{mn}v)}, \quad (1)$$

where M and N represent the number of elements in the x- and y-directions; A_{mn} and $\varphi(m,n)$ denote the equivalent amplitude and phase excitation of the element; x_{mn} and y_{mn} are the coordinates of the (m,n)-th element, $u = \sin\theta\cos\phi$, $v = \sin\theta\sin\phi$, and k is the wavenumber. $A_{mn} \cdot e^{j\varphi(m,n)}$ is the continuous excitation coefficient and should be implemented by digital metasurfaces. To this end, the discrete phase of each element is determined by a distinctive quantization probability, and the corresponding pattern is written as

$$F_0(\theta,\phi) = \sum_{m=1}^{M}\sum_{n=1}^{N} A'_{mn} \cdot e^{j\varphi_0(m,n)} \cdot e^{j(kx_{mn}u+ky_{mn}v)}, \quad (2)$$

where A'_{mn} is the prescribed amplitude excitation, while $\varphi_0(m,n)$ denotes the discrete random phase of each element. The fundamental principle of random phase approximation is designing the value of $\varphi_0(m,n)$ to guarantee the following equality:

$$\overline{F_0(\theta,\phi)} = F(\theta,\phi), \quad (3)$$

where the bar represents statistical averaging.

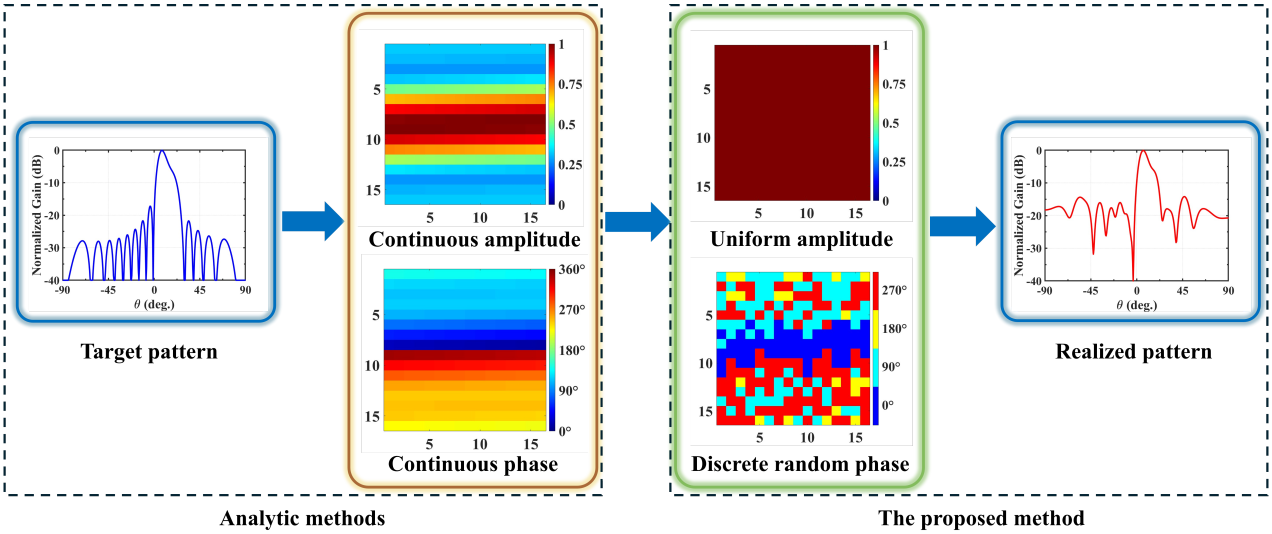

FIGURE 2. The schematic workflow of the proposed method.

The two excitation coefficients $A_{mn}\cdot e^{j\varphi(m,n)}$ in (1) and $A'_{mn}\cdot e^{j\varphi_0(m,n)}$ in (2) are decomposed into real and imaginary parts, respectively. Thus, (3) is fulfilled by the following conditions:

$$A_{mn}\cos\varphi(m,n)=A'_{mn}\overline{\cos\varphi_0(m,n)},\tag{4}$$

and

$$A_{mn}\sin\varphi(m,n)=A'_{mn}\overline{\sin\varphi_0(m,n)}.\tag{5}$$

In order to take full advantage of (4) and (5), the phase $\varphi_0(m,n)$ is decomposed as the product of two random and independent quantities [49]:

$$\varphi_0(m,n)=\eta(m,n)\xi(m,n).\tag{6}$$

To allow the proposed method to approximate continuous amplitude and phase simultaneously, we assume that $\eta(m,n)$ takes the values -1 or 1 with specific probabilities. As a result, the cosine function will not be influenced by $\eta(m,n)$. Accordingly, (4) and (5) are transformed as

$$A_{mn}\cos\varphi(m,n)=A'_{mn}\overline{\cos\xi(m,n)},\tag{7}$$

and

$$A_{mn}\sin\varphi(m,n)=A'_{mn}\overline{\sin\eta(m,n)\xi(m,n)}.\tag{8}$$

For simplicity, we denote

$$\cos\psi_{mn}=\overline{\cos\xi(m,n)},\tag{9}$$

where ψ_{mn} is the ideal continuous phase. In the case of a 2-bit phase-only digital metasurface, $\xi(m,n)$ can take any of the four discrete phases 0°, 90°, 180°, and 270° with certain probabilities to satisfy (9). However, to minimize the quantization error, we only choose the two discrete values adjacent to ψ_{mn}. The probability of taking the two values is determined in the following form:

$$\xi\left(m,n\right)=\begin{cases}\Delta\varphi\cdot\lfloor\psi_{mn}/\Delta\varphi\rfloor=\xi_1 & p_\xi(m,n)\\ \Delta\varphi\cdot\lfloor\psi_{mn}/\Delta\varphi\rfloor+\Delta\varphi=\xi_2 & 1-p_\xi(m,n),\end{cases}\tag{10}$$

where $\lfloor\psi_{mn}/\Delta\varphi\rfloor$ denotes the integer part of $\psi_{mn}/\Delta\varphi$; $\Delta\varphi$ is the phase quantization precision; and $p_\xi(m,n)$ means the quantization probability of $\xi(m,n)$. According to the definition of statistical averaging and (10), $\cos\xi(m,n)$ is expressed as

$$\overline{\cos\xi(m,n)}=p_\xi(m,n)\cos\xi_1+(1-p_\xi(m,n))\cos\xi_2\tag{11}$$

By substituting (11) into (7), we can get the value of $p_\xi(m,n)$:

$$p_\xi(m,n)=\frac{\cos\xi_2-A_{mn}\cdot\cos\varphi(m,n)/A'_{mn}}{\cos\xi_2-\cos\xi_1},\tag{12}$$

As mentioned before, the random quantity $\eta(m,n)$ in (8) is designed as

$$\eta(m,n)=\begin{cases}-1, & p_\eta(m,n)\\ +1, & 1-p_\eta(m,n),\end{cases}\tag{13}$$

with $p_\eta(m,n)$ representing the quantization probability of $\eta(m,n)$. After obtaining $\xi(m,n)$ through (10), we expand $\overline{\sin\eta(m,n)\xi(m,n)}$ as follows according to the definition of statistical averaging:

$$\begin{aligned}\overline{\sin\eta(m,n)\xi(m,n)}=&-p_\eta(m,n)p_\xi(m,n)\sin\xi_1\\&-p_\eta(m,n)(1-p_\xi(m,n))\sin\xi_2\\&+(1-p_\eta(m,n))(1-p_\xi(m,n))\sin\xi_2\\&+(1-p_\eta(m,n))p_\xi(m,n)\sin\xi_1.\end{aligned}\tag{14}$$

Subsequently, we substitute (14) into (8) to get the probability $p_\eta(m,n)$ as follows:

$$p_\eta(m,n)=\frac{A_{mn}\cdot\sin\varphi(m,n)/A'_{mn}}{2p_\xi(m,n)\cdot\sin\xi_1+2(1-p_\xi(m,n))\cdot\sin\xi_2}+\frac{1}{2}.\tag{15}$$

The two probabilities $p_\xi(m,n)$ and $p_\eta(m,n)$ should be constrained within the range from 0 to 1. Accordingly, we can get the following condition (see the detailed derivation in the Appendix A):

$$\frac{A_{mn}}{A'_{mn}} \leqslant \cos\left(\frac{\Delta\varphi}{2}\right), \tag{16}$$

which indicates that the phase quantization precision influences the performance of the proposed method. A_{mn} is normalized to the range from 0 to $A'_{mn}\cos(\Delta\varphi/2)$ when the value of A'_{mn} is fixed. It can be seen that A_{mn} is less restricted with the increase of the phase quantization precision, which is further discussed in Section 3.3.3.

Algorithm 1 Optimization Process of the Random Phase Approximation Method

```
Input:
Metasurface's parameters: $x_{mn}, y_{mn}$;
Target pattern's parameters: $A_{mn}, \varphi(m,n), F$;
Random quantities' parameters: $\eta_1, \eta_2, \xi_1, \xi_2, p_\eta, p_\xi$.
for $s = 1, \ldots, S$ do
    Calculate $\varphi_s$ using (10) and (13) as the $s$-th phase coding pattern.
    Calculate $F_s$ using (2) as the $s$-th realized pattern.
    Calculate $F_e(s) = |F - F_s|$ as the $s$-th error between the realized and the target pattern.
end for
Select $s^*$ that minimizes $F_e(s)$
output: The optimal pattern $F_{s^*}$ and the phase coding pattern $\varphi_{s^*}$.
```

The randomness of the proposed method indicates that a single realization of the pattern $F_0(\theta,\phi)$ may not provide an optimal approximation of the target pattern $F(\theta,\phi)$. Thus, we generate the random phase distribution of elements multiple times and select the optimal result, i.e., the one that minimizes the error between the realized and the target patterns. The pseudocode of the optimization process is summarized in Algorithm 1, where F is the target pattern. S is the number of computations. φ_s and F_s denote the s-th phase coding pattern and the realized pattern, respectively. $F_e(s) = |F - F_s|$ represents the s-th error between the realized and target pattern. The definition of the mean squared error (MSE) between the realized and target pattern is expressed as follows:

$$\sigma^2 = \overline{|F_0(\theta,\phi) - F(\theta,\phi)|^2}. \tag{17}$$

The above equation is further expanded in combination with (1), (2), and (6):

$$\begin{aligned}\sigma^2 = {} & \overline{\left|\sum_{m=1}^{M}\sum_{n=1}^{N} A'_{mn} b_{mn}\cos\xi(m,n)\right|^2} \\ & + \overline{\left|\sum_{m=1}^{M}\sum_{n=1}^{N} A'_{mn} b_{mn}\sin[\eta(m,n)\xi(m,n)]\right|^2} \\ & - \left|\sum_{m=1}^{M}\sum_{n=1}^{N} A_{mn} e^{j\varphi(m,n)} b_{mn}\right|^2, \end{aligned} \tag{18}$$

where b_{mn} represents $e^{j(kx_{mn}u + ky_{mn}v)}$ for simplicity. Since the random quantities $\xi(m,n)$ and $\eta(m,n)$ are uncorrelated, the three terms in (18) are expanded as

$$\begin{aligned} & \overline{\left|\sum_{m=1}^{M}\sum_{n=1}^{N} A'_{mn} b_{mn}\cos\xi(m,n)\right|^2} \\ = {} & \left|\sum_{m=1}^{M}\sum_{n=1}^{N} A'_{mn} b_{mn}\overline{\cos\xi(m,n)}\right|^2 \\ & + \sum_{m=1}^{M}\sum_{n=1}^{N} (A'_{mn})^2\overline{\cos^2\xi(m,n)} \\ & - \sum_{m=1}^{M}\sum_{n=1}^{N} (A'_{mn})^2\{\overline{\cos\xi(m,n)}\}^2, \end{aligned} \tag{19}$$

$$\begin{aligned} & \overline{\left|\sum_{m=1}^{M}\sum_{n=1}^{N} A'_{mn} b_{mn}\sin[\eta(m,n)\xi(m,n)]\right|^2} \\ = {} & \left|\sum_{m=1}^{M}\sum_{n=1}^{N} A'_{mn} b_{mn}\overline{\sin[\eta(m,n)\xi(m,n)]}\right|^2 \\ & + \sum_{m=1}^{M}\sum_{n=1}^{N} (A'_{mn})^2\overline{\sin^2\xi(m,n)} \\ & - \sum_{m=1}^{M}\sum_{n=1}^{N} (A'_{mn})^2\{\overline{\sin\eta(m,n)\xi(m,n)}\}^2, \end{aligned} \tag{20}$$

and

$$\begin{aligned} & \left|\sum_{m=1}^{M}\sum_{n=1}^{N} A_{mn} e^{j\varphi(m,n)} b_{mn}\right|^2 \\ = {} & \left|\sum_{m=1}^{M}\sum_{n=1}^{N} A'_{mn} b_{mn}\overline{\cos\xi(m,n)}\right|^2 \\ & + \left|\sum_{m=1}^{M}\sum_{n=1}^{N} A'_{mn} b_{mn}\overline{\sin[\eta(m,n)\xi(m,n)]}\right|^2, \end{aligned} \tag{21}$$

respectively. More details are presented in the Appendix B. Substituting (7) and (8) into (19) and (20) and combining (19), (20), and (21), we further reduce the MSE in (18) as

$$\sigma^2 = \sum_{m=1}^{M}\sum_{n=1}^{N}\left((A'_{mn})^2 - A_{mn}^2\right). \tag{22}$$

The normalized MSE of (22) is expressed as

$$\sigma_1^2 = \frac{\sum_{m=1}^{M}\sum_{n=1}^{N}\left((A'_{mn})^2 - A_{mn}^2\right)}{\left|\sum_{m=1}^{M}\sum_{n=1}^{N} A_{mn}\right|^2}. \tag{23}$$

The MSE comparison between this work and other random quantization methods will be presented and discussed in Section 3.2.

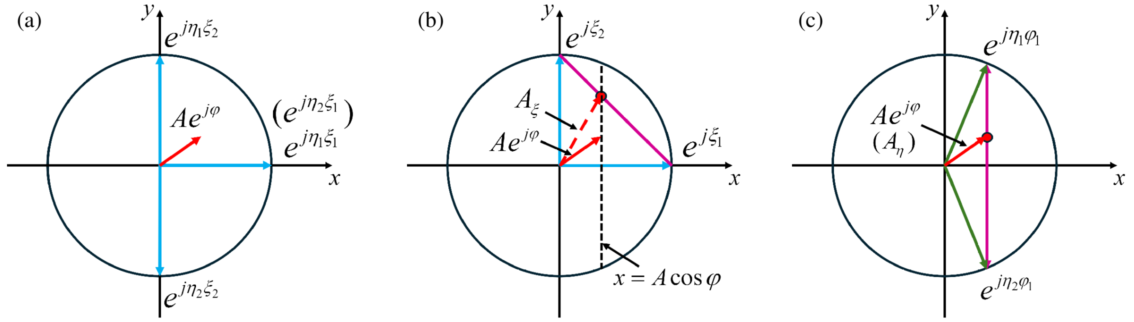

FIGURE 3. Vector representation of the proposed method. (a) ξ and η are both random quantities. The red vector represents $Ae^{j\varphi}$ with float amplitude and phase. The vectors $e^{j\eta_1\xi_1}$, $e^{j\eta_1\xi_2}$, $e^{j\eta_2\xi_1}$, and $e^{j\eta_2\xi_2}$ are the possible values of $e^{j\varphi_0}$, where $e^{j\eta_2\xi_1} = e^{j\eta_1\xi_1} = e^{j0}$. (b) ξ is random, while η is $+1$. A_ξ moves along the purple line segment when p_ξ varies from 0 to 1. $\text{Re}(A_\xi) = \text{Re}(Ae^{j\varphi}) = A\cos\varphi$ is achieved when p_ξ is set to $\cos\varphi$. (c) ξ is fixed as φ_1, while η is random, where $\cos\varphi_1 = A\cos\varphi$. A_η moves along the purple line segment when p_η varies from 0 to 1. $\text{Im}(A_\eta) = \text{Im}(Ae^{j\varphi}) = A\sin\varphi$ is achieved when p_η is set to $1/2(A\sin\varphi/\sin\varphi_1 + 1)$.

2.2. Principle of Simultaneous Amplitude and Phase Approximation

To explain how the proposed method simultaneously approximates the amplitude and phase distributions of elements, we transform (3) as follows:

$$E[e^{j\varphi_0}] = Ae^{j\varphi}, \tag{24}$$

where A and φ represent the continuous amplitude and phase of elements, while φ_0 denotes the random phase calculated by the proposed method. $E[e^{j\varphi_0}]$ is the statistical average of $e^{j\varphi_0}$. φ_0 is decomposed as two random quantities ξ and η through (6). For simplicity, we assume that the continuous phase φ ranges from 0° to 90°. In the case of a 2-bit phase-only digital metasurface, η takes the values $\eta_1 = +1$ and $\eta_2 = -1$, and ξ takes the two discrete values adjacent to φ, i.e., $\xi_1 = 0°$ and $\xi_2 = 90°$, as determined by (10) and (13).

To illustrate the relationship between $e^{j\varphi_0}$ and $Ae^{j\varphi}$ intuitively, we plot them as vectors on the unit circle in Fig. 3(a), where x-axis and y-axis denote the real and imaginary parts, respectively. The red vector represents $Ae^{j\varphi}$ with float amplitude and phase, with the three blue vectors denoting all possible values of the random phase $e^{j\varphi_0}$. Since η takes the values $\eta_1 = +1$ and $\eta_2 = -1$, $(e^{j\eta_1\xi_1}, e^{j\eta_1\xi_2})$ and $(e^{j\eta_2\xi_1}, e^{j\eta_2\xi_2})$ are symmetric with respect to the x-axis. Moreover, $e^{j\eta_2\xi_1}$ coincides with $e^{j\eta_1\xi_1}$, as both are equal to e^{j0}. $E[e^{j\varphi_0}]$ is the statistical average of the vectors $e^{j\eta_1\xi_1}$, $e^{j\eta_1\xi_2}$, $e^{j\eta_2\xi_1}$, and $e^{j\eta_2\xi_2}$ with respect to the random quantities ξ and η. The influences of ξ and η on $E[e^{j\varphi_0}]$ are investigated as follows.

First, we assume that η is fixed as $+1$ and ξ is random. In this case, only the vectors $e^{j\xi_1}$ and $e^{j\xi_2}$ are considered, and $E[e^{j\varphi_0}]$ is transformed as

$$A_\xi = p_\xi e^{j\xi_1} + (1 - p_\xi)e^{j\xi_2}, \tag{25}$$

where A_ξ represents the statistical average of the two vectors $e^{j\xi_1}$ and $e^{j\xi_2}$ with respect to ξ. As shown in Fig. 3(b), when p_ξ varies from 0 to 1, the red dashed vector A_ξ moves along the purple line segment. The black dashed line corresponds to all vectors whose real part is $A\cos\varphi$. It can be seen that the variation of p_ξ influences both the real and imaginary parts of A_ξ. In this case, we only need to set $p_\xi = \cos\varphi$ such that the real part of A_ξ satisfies $\text{Re}(A_\xi) = A\cos\varphi$.

Next, we assume that ξ is fixed as φ_1, where $\cos\varphi_1 = A\cos\varphi$. While ξ is discrete in the proposed method, it is set to a specific continuous value here for the sake of illustration. In this case, the green vectors $e^{j\eta_1\varphi_1}$ and $e^{j\eta_2\varphi_1}$ are considered, and $E[e^{j\varphi_0}]$ is transformed as

$$A_\eta = p_\eta e^{j\eta_1\varphi_1} + (1 - p_\eta)e^{j\eta_2\varphi_1}, \tag{26}$$

where A_η represents the statistical average of the two vectors $e^{j\eta_1\varphi_1}$ and $e^{j\eta_2\varphi_1}$ with respect to η. As shown in Fig. 3(c), when p_η varies from 0 to 1, A_η moves along the purple line segment. It can be seen that the variation of p_η primarily influences the imaginary part of A_η without affecting its real part. Specifically, we set $p_\eta = 1/2(A\sin\varphi/\sin\varphi_1 + 1)$ such that the imaginary part of A_η satisfies $\text{Im}(A_\eta) = A\sin\varphi$. In this case, A_η coincides with $Ae^{j\varphi}$.

Overall, the two random quantities ξ and η respectively influence the real and imaginary parts of $E[e^{j\varphi_0}]$. By appropriately adjusting the probabilities of ξ and η, we find that the value of $E[e^{j\varphi_0}]$ almost covers the entire unit circle. This indicates that the proposed method can approximate nearly all continuous amplitudes and phases of elements.

3. RESULTS

3.1. Numerical Examples

To demonstrate the performance of the proposed method, a digital metasurface consisting of 16×16 elements with 2-bit phase responses of 0°, 90°, 180°, and 270° is taken as the hardware. The size of the metasurface element is $0.48 \times 0.48 \times 0.09\lambda_0^3$ at 11 GHz. The continuous excitation coefficients obtained from three analytic methods are approximated by the proposed method, and the generated discrete phase distributions can be implemented on the hardware to realize three types of complex beams. For simplicity, the amplitude of each metasurface element is fixed as 1 in the following numerical examples.

3.1.1. Cosecant Beam

In the first example, a cosecant beam is designed. Specifically, the beam varies between $\theta = 8°$ and $\theta = 20°$ in the $\phi = 0°$ plane. The Woodward-Lawson method is utilized to calculate

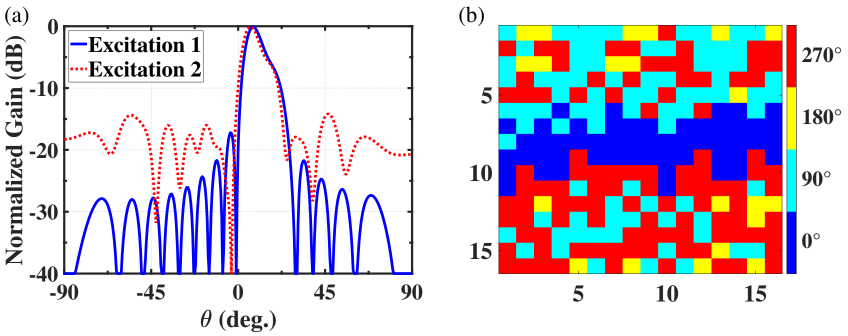

FIGURE 4. Numerical results of the cosecant beam at 11 GHz: (a) the patterns generated from metasurfaces with Excitation 1 and Excitation 2. Excitation 1 denotes the continuous amplitude and phase, while Excitation 2 represents the discrete random phase; (b) The calculated coding pattern of the metasurface giving the cosecant beam with random phase approximation.

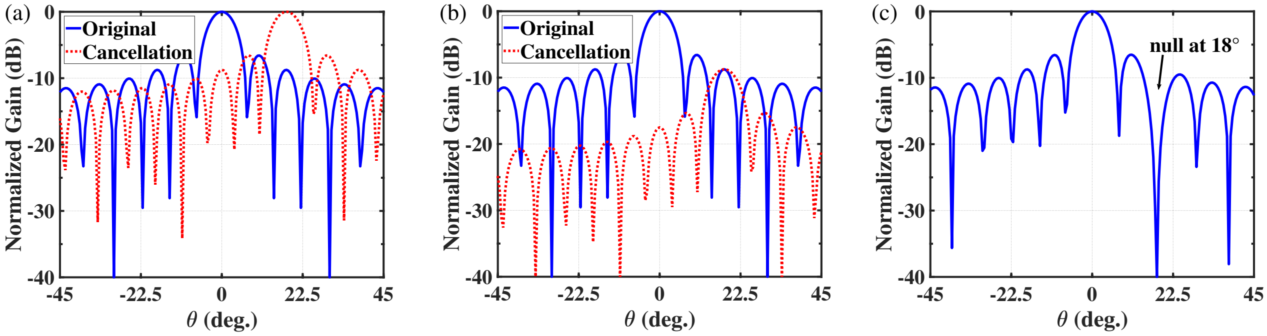

FIGURE 5. The process of forming a radiation pattern at 11 GHz with a prescribed null at 18°. (a) The original and cancellation pattern. (b) The cancellation pattern is multiplied by the coefficient γ_1. (c) The final pattern with a null at 18°.

the continuous excitation coefficients. The Woodward-Lawson method regards the desired cosecant beam as the superposition of multiple linear arrays. The excitation coefficients of these linear arrays are added, yielding the continuous amplitude and phase for each corresponding element [26].

The obtained continuous amplitude and phase distribution is approximated by the proposed method to obtain the desired discrete phase distribution. The specific process is as follows: First, the two quantization probabilities $p_\xi(m,n)$ and $p_\eta(m,n)$ are derived as (12) and (15). Then, the discrete phase distributions are obtained as (10) and (13). Finally, the beams are calculated as (1) and (2). It should be noted that all the following radiation pattern gains are normalized, as the primary contribution of this work is the random phase approximation method, and the radiation patterns are only provided for verification. As illustrated in Fig. 4(a), the blue solid line represents the cosecant beam corresponding to the excitation with the continuous amplitude and phase, while the red dashed line depicts the beam corresponding to the excitation with the discrete random phase. The two beams match well in the range between 8° and 20°. The side lobe level of the beam with discrete random phase excitation is -14.2 dB, which is 3.1 dB higher than that of the beam with continuous amplitude and phase excitation. The higher side lobe can be attributed to the limited modulation capability of 2-bit phase-only digital metasurfaces, which cannot achieve precise beamforming and low side lobe levels simultaneously. The phase coding pattern of the metasurface is shown in Fig. 4(b).

3.1.2. Beam Scanning with the Prescribed Null

In the second example, beams with prescribed nulls are considered due to their wide application in radar and communications. The null steering synthesis method in [50] is utilized to calculate the continuous excitation coefficients. This method generates a prescribed null by subtracting a scaled cancellation pattern from an original pattern, as detailed below. Fig. 5(a) demonstrates that the method starts from a given original pattern $F_0(\theta)$ and a cancellation pattern $F_c(\theta)$ in the direction $\theta_n = 18°$. Fig. 5(b) illustrates the scaled cancellation pattern $\gamma_1 F_c(\theta)$ where $\gamma_1 = F_0(\theta_n)/F_c(\theta_n)$. Finally, Fig. 5(c) shows that the final pattern is determined by the subtraction of $\gamma_1 F_c(\theta)$ from $F_0(\theta)$, yielding a prescribed null. Furthermore, it is possible to generate multiple prescribed nulls on the original pattern. The pattern with L null angles is represented as follows [50]:

$$F(\theta) = F_0(\theta) - \sum_{l=1}^{L} \gamma_l \sum_{n=1}^{N} e^{j(n-1)kd(\cos\theta - \cos\theta_l)}. \tag{27}$$

The excitation coefficient of each element is derived from (27) using the inverse Fourier transform

$$a_n = a_{0n} - \sum_{l=1}^{L} \gamma_l e^{-j(n-1)kd\cos\theta_l}. \tag{28}$$

where a_{0n} denotes the excitation coefficient that generates the original pattern.

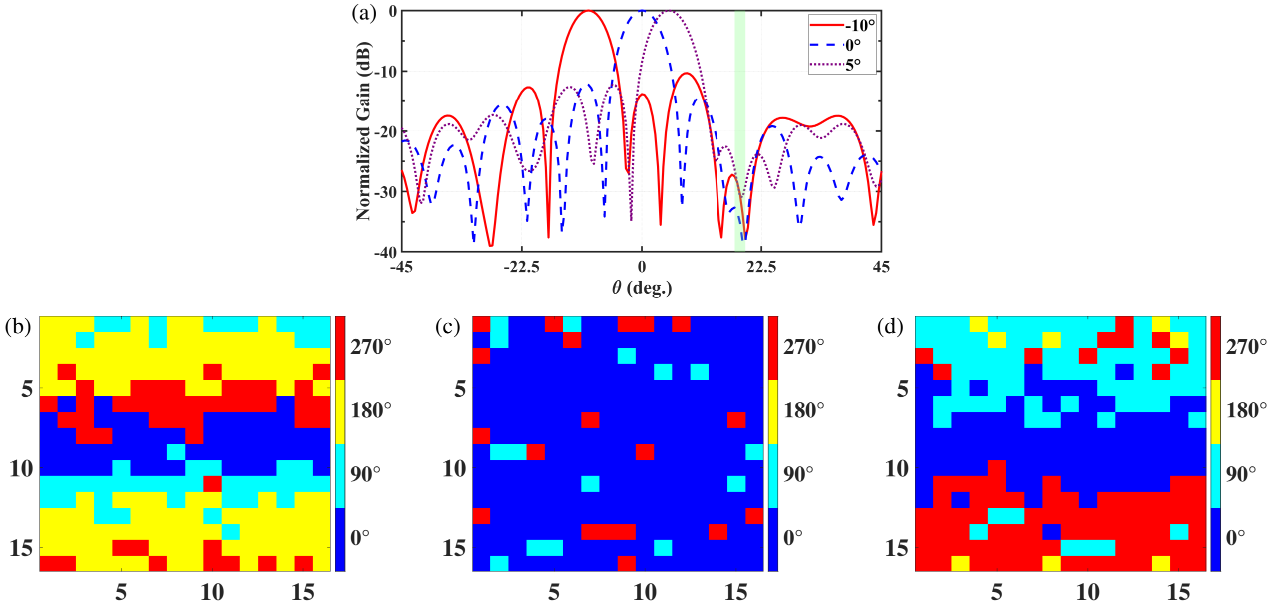

FIGURE 6. Numerical results of the beam at 11 GHz with a prescribed null at 18°: (a) Simulated beams; (b), (c), and (d) the calculated coding patterns with main beams pointing at $-10°$, $0°$, and $5°$, respectively.

The random phase distribution is calculated to approximate the continuous excitation coefficients yielded by the above method. The results are demonstrated in Fig. 6(a). It can be seen that as the beam scans from $\theta = -10°$ to $\theta = 5°$ in the $\phi = 0°$ plane, a prescribed null remains near $\theta_n = 18°$ with its normalized level below -25 dB. The phase coding patterns of the metasurface are shown in Figs. 6(b)–(d), respectively. The simulations illustrate the effectiveness of the proposed method.

3.1.3. Flat-Top Beam

In the last example, the target pattern is a flat-top beam. Specifically, the main lobe region is fixed between $\theta = 8°$ and $\theta = 20°$ in the $\phi = 30°$ plane. The continuous excitation coefficient a_{mn} is obtained from the two-dimensional inverse Fourier transform as follows:

$$a_{mn} = \int_0^{2\pi} \int_0^{\pi/2} F(\theta, \phi) e^{j(kx_{mn}u + ky_{mn}v)} d\theta d\phi. \qquad (29)$$

The resultant a_{mn} is approximated by the proposed method to obtain the discrete random phase distribution. As illustrated in Fig. 7, the patterns of the flat-top beams generated by the two excitations are shown in Figs. 7(a) and 7(b). It can be seen that the two results show good consistency. The side lobe level of the pattern with discrete random phase excitation is -9.8 dB, being 9.5 dB higher than that of the pattern with continuous amplitude and phase excitation. This is attributed to the fact that the excitation coefficient obtained from the inverse Fourier transform includes amplitude tapering, whereas the digital metasurface in this work provides uniform amplitude distribution across all elements. The phase coding pattern of the metasurface is shown in Fig. 7(d). The example confirms the effectiveness of the proposed method in beam synthesis.

3.2. Comparison with Stochastic Optimization and Other Phase Quantization Methods

Stochastic optimization methods can also provide discrete phase distributions that generate complex beams. To demonstrate the advantages of the proposed method, we compare it with stochastic optimization methods. The flat-top beam is utilized as an illustrative example. The array in the comparison is the same as that in Section 3.1. The fitness function for stochastic optimization is defined as

$$fitness = c_1 \cdot \overline{|MLL - MLL_0|} + c_2 \cdot \max|SLL - SLL_0|, \qquad (30)$$

where c_1 and c_2 are the weighting coefficients; MLL is the main lobe level of the flat-top region; and SLL is the side lobe level of the other regions. The coefficient c_1 weights the flatness of the main lobe region, while c_2 influences the maximum side lobe level. We find that a large c_1/c_2 leads to a significant increase in side lobe levels, whereas a small c_1/c_2 causes fluctuations within the main lobe. Thus, we perform multiple adjustments of c_1 and c_2 to achieve satisfactory performance. The values of c_1 and c_2 are set as $c_1 = 1.1$ and $c_2 = 0.45$, respectively.

The main lobe region of $MLL_0 = 0$ dB is fixed between $\theta = 8°$ and $\theta = 20°$ in the $\phi = 0°$ plane. The side lobe level is constrained to a maximum of $SLL_0 = -15$ dB. The main lobe and side lobe levels of the desired pattern are dictated by the design requirements and the practical capabilities of the metasurface. The comparison of the flat-top beam patterns generated by GA, PSO, and the proposed method is illustrated in Fig. 8. The detailed performance is presented in Table 1, where the half-power beam width (HPBW) of the three methods shows slight discrepancies. Although GA and PSO achieve slightly lower side lobe levels than the proposed method, they require significantly longer optimization time than the latter. Overall, the

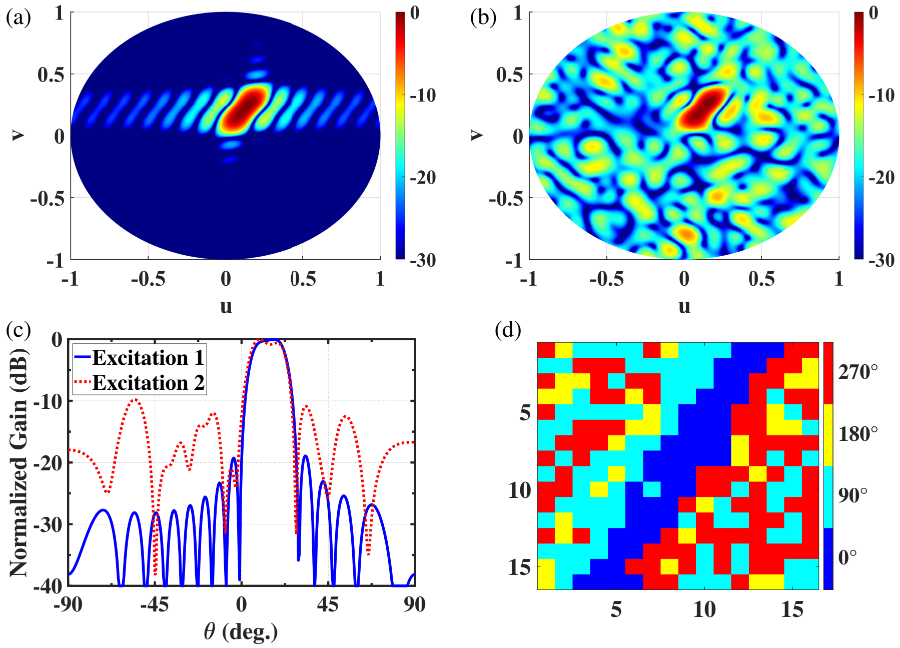

FIGURE 7. Numerical results of the flat-top beam at 11 GHz: (a) Far-field patterns generated by metasurfaces with continuous amplitude and phase and (b) Far-field patterns generated by metasurfaces with discrete random phase; (c) Comparison between the two results. Excitation 1 denotes the continuous amplitude and phase, while Excitation 2 represents the discrete random phase; (d) The calculated coding pattern of the metasurface with random phase approximation.

TABLE 1. Comparison of the proposed method with optimization algorithms.

Method	HPBW (deg.)	Side lobe level (dB)	Optimization time (s)
PSO	18.2	−10.7	1674
GA	18.4	−12.1	1243
This work	17.55	−9.79	1.31

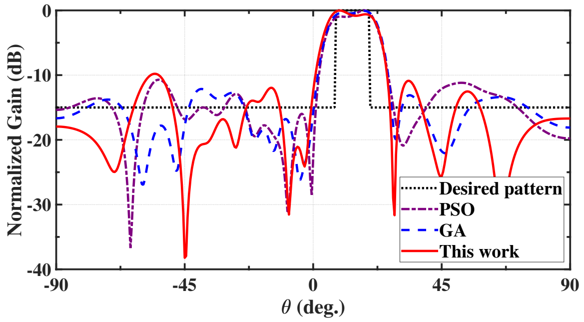

FIGURE 8. Comparison of flat-top beams generated by stochastic optimizations and the proposed method at 11 GHz.

proposed method exhibits satisfactory performance with minimal time.

To clarify the differences between the proposed method and other random quantization methods, we take the pencil beam and flat-top beam in the $\phi = 0°$ plane as examples. The array in the comparison is still the same as that in Section 3.1. For pencil beam generation, the main lobe direction is controlled solely by the phase variation across the array, without any amplitude modulation. Therefore, in the case of phase-only approximation, the proposed method is equivalent to the 2PV method, that is, $\eta(m, n)$ in (6) is fixed as $+1$. The comparison of the pencil beam along $\theta = -20°$ is shown in Fig. 9(a), where the target beam is generated by the continuous phase distribution. Random quantization methods, including the 2PV, 3PV, and the proposed method, are subsequently employed to approximate the target beam. These methods effectively reduce the beam pointing deviation and side lobe level. Furthermore, the comparison of the flat-top beam is shown in Fig. 9(b), where the target beam is generated by the continuous amplitude and phase distribution with the main lobe region fixed between $\theta = -8°$ and $\theta = 8°$ in the $\phi = 0°$ plane. For flat-top beam generation, each element has distinct amplitude and phase responses. The phase determines the beam direction while the amplitude shapes the beam envelope. However, the 2PV and 3PV methods are limited to approximating the phase. Consequently, their beamforming performance is significantly degraded. In contrast, the proposed method agrees well with the target beam.

Furthermore, to quantitatively evaluate the performance of the proposed method in flat-top beam synthesis, we compute the MSE between the beams generated by these random quantization methods and the target beam for different numbers of elements. As illustrated in Fig. 10, the results are normalized to the maximum MSE among all the compared methods. It can be observed that the proposed method consistently exhibits lower normalized MSE than the 2PV and 3PV methods. These results indicate that the proposed method achieves enhanced beamforming performance, as it can approximate continuous amplitude and phase distributions of elements simultaneously.

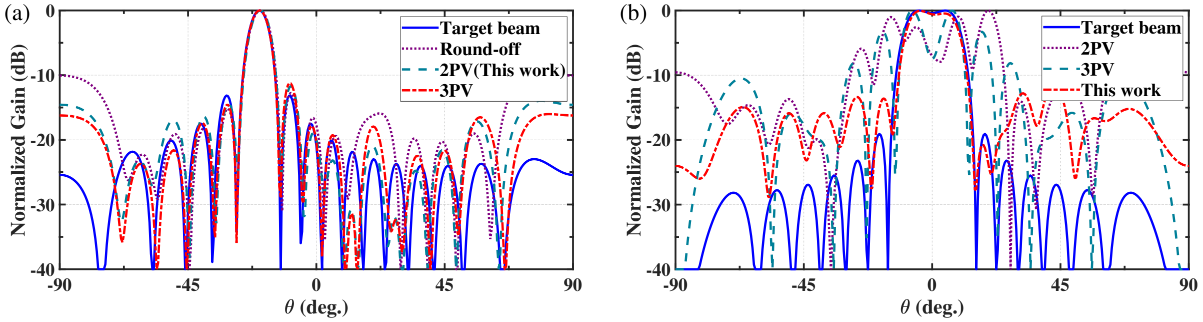

FIGURE 9. Comparison of (a) pencil beams and (b) flat-top beams generated by different quantization methods. The frequency is 11 GHz.

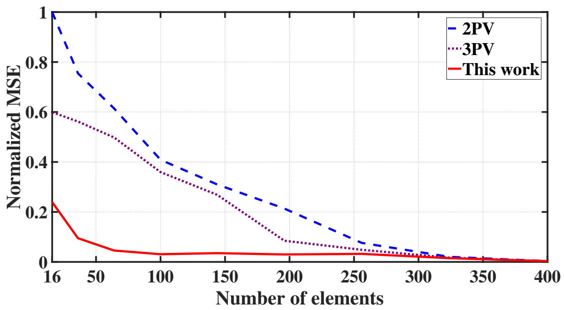

FIGURE 10. Comparison of the normalized MSE between the beams generated by random quantization methods and the target beam.

3.3. Full-Wave Simulations

3.3.1. The Metasurface

The metasurface element in [51] ($0.48 \times 0.48 \times 0.09\lambda_0^3$ at 11 GHz) is utilized to validate the numerical results in Section 3.1. The geometrical configuration of the metasurface element is presented in Fig. 11. The element consists of four parts, including the radiation layer, the ground planes, the direct current (DC) bias layer, and the feed network layer. The four parts are laminated together with two pieces of 0.2 mm thick Rogers RO4450F ($\varepsilon_r = 3.7$, $\tan\delta = 0.004$).

The top radiation layer consists of two identical patches and a small square patch with a metal via. The radiation patch is an equivalent magnetic dipole with a wide HPBW and is suitable for complex beam generation. Two PIN diodes are located in the gaps of the radiation patch, with their ON and OFF states switched by voltage modulation. When the two PIN diodes are respectively in the ON state, the surface current exhibits the same magnitude but opposite directions, producing a 180° phase difference. The feed network is composed of a two-port reflection-type phase shifter (RTPS) that integrates two PIN diodes. When both PIN diodes are in the ON state, the carefully designed microstrip line provides a 90° phase shift relative to the OFF state. The combination of the top radiation layer and RTPS then allows for the realization of 2-bit phase responses.

The digital metasurface for full-wave simulations is composed of 16×16 elements. The feed network is carefully designed to ensure the uniform distribution of energy across all ports.

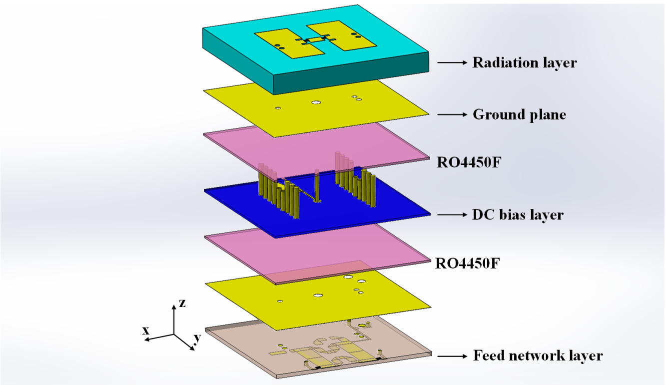

FIGURE 11. Geometrical configuration of the metasurface element based on [51].

3.3.2. Full-Wave Simulation Results

The cosecant, prescribed null and flat-top patterns in the $\phi = 0^\circ$ plane are simulated in CST Microwave Studio. The result of the cosecant beam is represented in Fig. 12(a), which agrees with the numerical result. The side lobe level remains below -14 dB. The results of scanning beams with a prescribed null at $\theta_n = 18^\circ$ are demonstrated in Fig. 12(b). As depicted, the difference between the full-wave and numerical results is negligible. Although the normalized gain at the prescribed null with the main beam pointing at -10°, 0°, and 5° is slightly higher than the numerical result, it remains below -25 dB. The result of the flat-top beam is shown in Fig. 12(c). The target main lobe region is fixed between $\theta = 8^\circ$ and $\theta = 20^\circ$, generally agreeing with the numerical result. The side lobe level is below -10 dB. The difference in the side lobe range depicted in Fig. 12 can be explained as follows. The numerical result is based on the point-source model, without considering the mutual coupling between adjacent metasurface elements, which affects the beamforming performance of the digital metasurface.

3.3.3. Parametric Study

A parametric study is necessary to examine the impact of varying numbers of elements and phase quantization precision on the performance of the proposed method. To this end, full-wave simulations of the flat-top beam are performed under these dif-

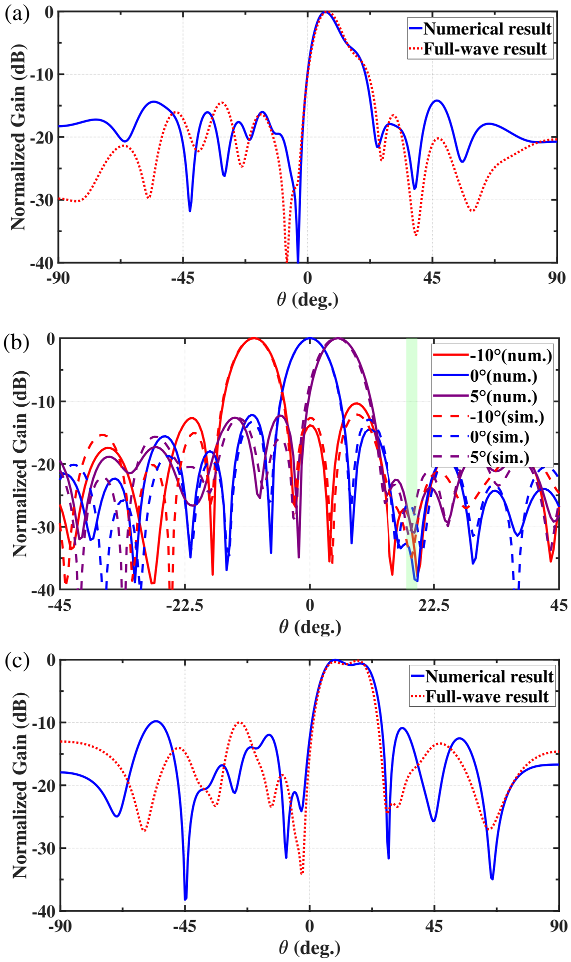

FIGURE 12. The numerical and full-wave results of patterns with (a) cosecant beam, (b) prescribed null, and (c) flat-top beam at 11 GHz.

ferent factors. For all the cases, the target main lobe region is fixed between $\theta = 8^\circ$ and $\theta = 20^\circ$ in the $\phi = 0^\circ$ plane. As shown in Fig. 13(a), a larger array provides greater flexibility and precision for the proposed method when the target main lobe region is fixed. (16) indicates that the continuous amplitude A_{mn} derived from analytic methods is subject to the amplitude constraint, i.e., A_{mn} is normalized to the range from 0 to $\cos(\Delta\varphi/2)$, since A'_{mn} is fixed as 1. When A_{mn} satisfies the amplitude constraint in (16), the performance is improved with the increase of the phase quantization precision, as shown in Fig. 13(b). Moreover, when $\Delta\varphi$ is fixed as 90°, the comparison between the cases in which A_{mn} is or is not subject to the amplitude constraint in (16) is shown in Fig. 13(c). It can be observed that the performance is slightly deteriorated when (16) is not satisfied. The two comparisons in Figs. 13(b) and 13(c) indicate that the performance is improved when A_{mn} satisfies the constraint in (16) and the phase quantization precision increases, which is in accordance with the analysis of (16) in Section 2.1.

3.4. Experimental Measurement

To further verify the proposed method, the flat-top, cosecant, and dual-beam patterns in the $\phi = 0^\circ$ plane are experimentally measured. Unlike the simulations, a smaller array with 8×8 elements is employed in the experiment, which is sufficient to validate the effectiveness of the proposed method. The effective size of the metasurface is $104 \times 104\,\text{mm}^2$ ($3.8 \times 3.8\lambda_0^2$ at 11 GHz), and the total size increases to $144 \times 144\,\text{mm}^2$ for DC bias and assembly. The experimental measurements of the metasurface were performed in an anechoic chamber, as shown in Fig. 14. The digital metasurface was excited through a coaxial port. Besides, the field-programmable gate array (FPGA) control board provided dynamic biasing voltages for the 2-bit digital metasurface, and commands were transmitted from the laptop via the I/O port. A linearly polarized horn antenna was connected to a vector network analyzer (Keysight N5230C) to receive the signal.

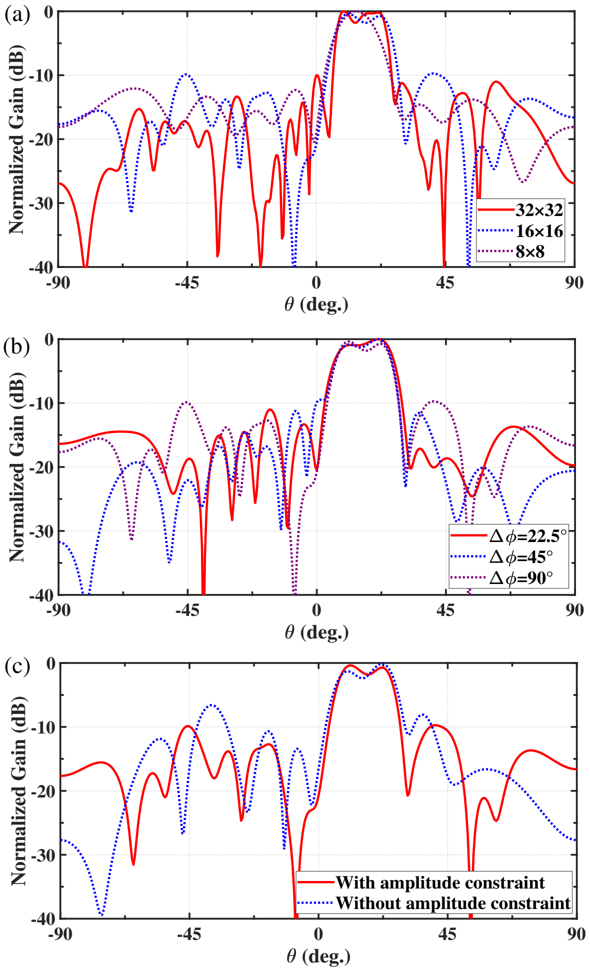

FIGURE 13. The flat-top beams with different (a) numbers of elements, (b) phase quantization precision at 11 GHz, and (c) comparison between the cases in which A_{mn} is subject to or not subject to the amplitude constraint in (16).

As shown in Fig. 15(a), the measured flat-top beam at 11 GHz is in general agreement with the simulation result. The HPBW is 38.5° (from -22.25° to 16.25°), being slightly narrower than the simulated value. The side lobe level is -6.35 dB, being 2.4 dB higher than the simulated value. In Figs. 15(b) and 15(c), the measured cosecant and dual-beam patterns agree well with the simulation results. The side lobe levels of the measured cosecant and dual-beam are 2.3 dB and

TABLE 2. Comparison of different realizations of flat-top beams.

Reference	Frequency (GHz)	Size (λ_0^2)	Antenna type	Method	Computational complexity	Reconfigurability
[33]	5.74	13.12	Phased array	Woodward-Lawson	Low	No
[34]	5.2	4.3	Transmitarray	Phase compensation	Low	No
[39]	11.1	7.1	Transmitarray	PSO	High	No
[41]	10	4.88	Transmitarray	GA	High	No
[43]	10	10	Reconfigurable transmitarray	GA	High	Yes
This work	11	3.8	Digital metasurface	Random phase	Low	Yes

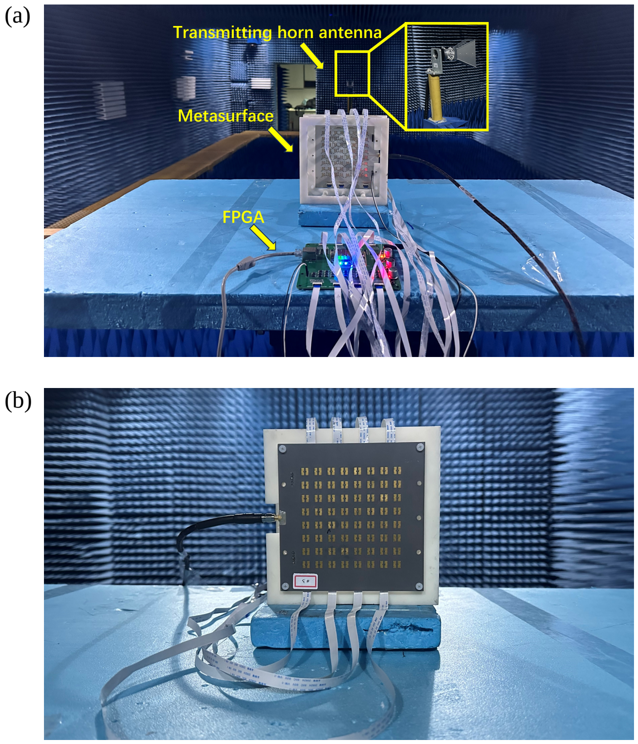

FIGURE 14. Far-field measurements. (a) Back view, (b) front view.

1.84 dB higher than the simulated values, respectively. Nevertheless, the curves in the other regions agree well with the simulations, validating the effectiveness of the proposed method. The higher side lobes in the measured results can be explained as follows. The SMA connector introduces extra loss in the experiment. Moreover, the errors in the fabrication of the digital metasurface contribute to additional loss.

To justify the novelty and advantages of the proposed method, it is compared with previous works in the field of complex beam synthesis. The flat-top beam is used as an illustrative example, and the results are summarized in Table 2. References [33] and [34] utilize analytic methods to design the excitation coefficients of the array elements, while References [39, 41], and [43] used stochastic optimization methods to generate flat-top beams. The comparison focuses on two aspects: reconfigurability and computational complexity.

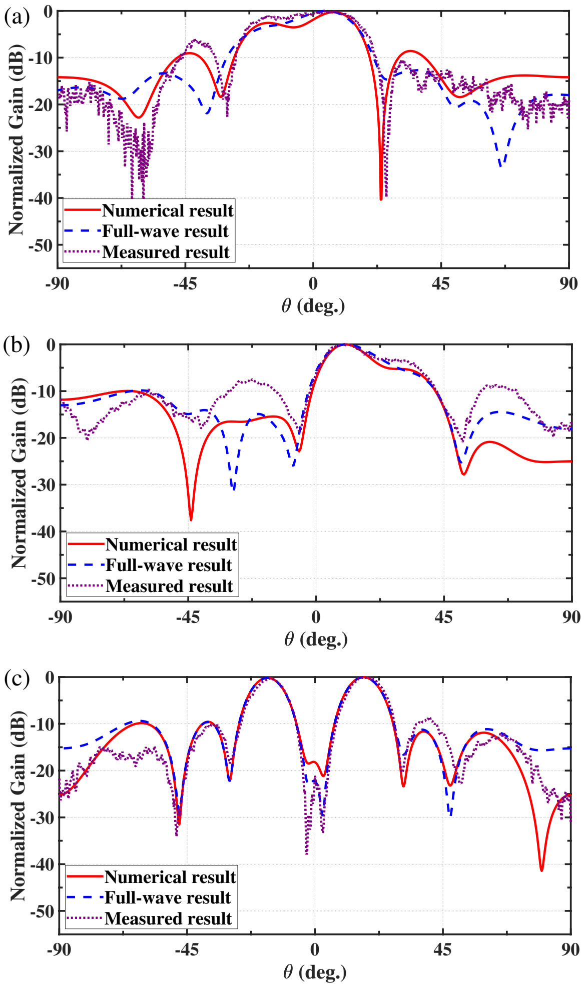

FIGURE 15. Measured beams of the 2-bit digital metasurface with 8 × 8 elements at 11 GHz, using the phase codes obtained by the proposed method. (a) Flat-top beam. (b) Cosecant beam. (c) Dual-beam.

The analytic methods, such as Woodward-Lawson in [33] and phase compensation in [34], are first discussed. These methods rapidly provide the continuous excitation coefficients of each element for complex beam synthesis. However, it is difficult to implement the calculated continuous distribution in digital metasurfaces, which require discrete excitations. On the contrary, the proposed method generates discrete random phase distributions that approximate continuous excitation coefficients, thereby enabling a complex beam reconfigurability on digital metasurfaces.

The existing stochastic optimization methods in reference [39], [41], and [43] can flexibly provide continuous or discrete excitation coefficients of each element to realize complex beams. Nevertheless, they suffer from extensive computational complexity. Compared to them, the proposed method significantly reduces computational complexity while avoiding the fine-tuning of optimization parameters, which is particularly suitable for dynamic complex beam synthesis.

4. CONCLUSION

A random phase approximation method is first proposed to rapidly and effectively realize complex beams in combination with digital metasurfaces. It is demonstrated that discrete random phases with specific quantization probability distributions can approximate a continuous amplitude and phase excitation. Several numerical examples are provided to evaluate the effectiveness and accuracy of the proposed method. Practical metasurfaces are utilized to validate the numerical and full-wave simulations. The metasurface shows excellent performance and adaptability under different complex beams. Overall, the proposed method provides a simple and effective way to realize complex beams. It can be extended to the terahertz, optical, and acoustic regimes with the exploration of different implementations.

ACKNOWLEDGEMENT

This work was supported by the National Natural Science Foundation of China (62171124, 62288101, 62225108, 62471134 and 62201139), National Key Laboratory of Space Target Awareness (STA2024ZCA0305), the Major Project of the Natural Science Foundation of Jiangsu Province (BK20212002), the Jiangsu Science and Technology Research Plan (BK20243028), the 111 Project (111-2-05), the Fundamental Research Funds for the Central Universities (2242022k60003, 2242024RCB0005).

APPENDIX A. DETAILED DERIVATION OF (16)

By substituting (7) into (12), we get the quantization probability $p_\xi(m,n)$ as follows:

$$p_\xi(m,n)=\frac{\cos\xi_2-\overline{\cos\xi(m,n)}}{\cos\xi_2-\cos\xi_1}. \tag{A1}$$

The statistical average $\overline{\cos\xi(m,n)}$ necessarily lies between $\cos\xi_1$ and $\cos\xi_2$. Therefore, $p_\xi(m,n)$ is always constrained between 0 and 1.

The quantization probability $p_\eta(m,n)$ is constrained to the range of $0\sim 1$ through the following condition:

$$\frac{A_{mn}\cdot\sin\varphi(m,n)/A'_{mn}}{p_\xi(m,n)\cdot\sin\xi_1+(1-p_\xi(m,n))\cdot\sin\xi_2}-1\leqslant 0. \tag{A2}$$

The value of $p_\xi(m,n)$ is substituted into (A2). A_{mn}/A'_{mn} is represented by c for simplicity. The denominator is then expanded as

$$\begin{aligned}&p_\xi(m,n)\cdot\sin\xi_1+(1-p_\xi(m,n))\cdot\sin\xi_2\\ =&\frac{\cos\xi_2\sin\xi_1-\cos\xi_1\sin\xi_2}{\cos\xi_2-\cos\xi_1}\\ &+\frac{c\cdot\cos\varphi(m,n)(\sin\xi_2-\sin\xi_1)}{(\cos\xi_2-\cos\xi_1)}.\end{aligned} \tag{A3}$$

The trigonometric identities employed in this analysis are

$$\cos\xi_2-\cos\xi_1 = -2\sin\left(\frac{\xi_2+\xi_1}{2}\right)\sin\left(\frac{\xi_2-\xi_1}{2}\right), \tag{A4}$$

$$\sin(\xi_1-\xi_2) = 2\sin\left(\frac{\xi_1-\xi_2}{2}\right)\cos\left(\frac{\xi_1-\xi_2}{2}\right). \tag{A5}$$

The condition in (A2) is then transformed as

$$\frac{c\cdot\cos(\varphi(m,n)-\frac{\xi_1+\xi_2}{2})-\cos\frac{\Delta\varphi}{2}}{\cos\frac{\Delta\varphi}{2}-c\cdot\cos(\frac{\xi_1+\xi_2}{2})\cos\varphi(m,n)}\leqslant 0, \tag{A6}$$

where $\cos\Delta\varphi/2$ is greater than 0 since $\Delta\varphi$ is less than π. The following condition is derived from (10)

$$\cos\varphi(m,n)\approx\cos\frac{\xi_1+\xi_2}{2}, \tag{A7}$$

which means $\cos(\varphi(m,n)-(\xi_1+\xi_2)/2)$ is greater than 0. Since the maximum value of $\cos((\xi_1+\xi_2)/2)$ is $\cos\Delta\varphi/2$ and c is less than 1, $\cos\Delta\varphi/2$ is always greater than $c\cdot\cos((\xi_1+\xi_2)/2)\cos\varphi(m,n)$. Thus, (A6) is transformed as

$$c\cdot\cos\left(\varphi(m,n)-\frac{\xi_1+\xi_2}{2}\right)-\cos\frac{\Delta\varphi}{2}\le 0, \tag{A8}$$

which should be satisfied for all values of m and n. Since $\cos(\varphi(m,n)-(\xi_1+\xi_2)/2)$ is less than 1, (A8) is reduced as

$$c\le\cos\left(\frac{\Delta\varphi}{2}\right), \tag{A9}$$

which is (16) in the main text.

APPENDIX B. DETAILED DERIVATION OF (19)

In Equation (19), the statistical averaging depends on the value of $\xi(m,n)$. We can transform (19) into a symmetrical form as follows:

$$\begin{aligned}&\overline{\left|\sum_{m=1}^{M}\sum_{n=1}^{N}A'_{mn}b_{mn}\cos\xi\left(m,n\right)\right|^2}\\ &-\left|\sum_{m=1}^{M}\sum_{n=1}^{N}A'_{mn}b_{mn}\overline{\cos\xi(m,n)}\right|^2\\ =&\sum_{m=1}^{M}\sum_{n=1}^{N}(A'_{mn})^2\overline{\cos^2\xi\left(m,n\right)}\end{aligned}$$

$$-\sum_{m=1}^{M}\sum_{n=1}^{N}(A'_{mn})^2\{\overline{\cos\xi(m,n)}\}^2. \tag{B1}$$

Both sides of this equation are consistent with the definition of the variance. Accordingly, the left-hand side of (B1) is transformed as

$$\begin{aligned}&\overline{\left|\sum_{m=1}^{M}\sum_{n=1}^{N}A'_{mn}b_{mn}\cos\xi\left(m,n\right)\right|^2}\\&-\left|\sum_{m=1}^{M}\sum_{n=1}^{N}A'_{mn}b_{mn}\overline{\cos\xi(m,n)}\right|^2\\&=\mathrm{Var}\left(\sum_{m=1}^{M}\sum_{n=1}^{N}X_{mn}\right),\end{aligned} \tag{B2}$$

where Var() denotes the variance, and $|A'_{mn}b_{mn}\cos\xi(m,n)|$ is represented by X_{mn} for simplicity. According to the relationship between variance and covariance, (B2) is expanded as

$$\begin{aligned}&\mathrm{Var}\left(\sum_{m=1}^{M}\sum_{n=1}^{N}X_{mn}\right)\\&=\sum_{m_1,m_2=1}^{M}\sum_{n_1,n_2=1}^{N}\mathrm{Cov}(X_{m_1n_1},X_{m_2n_2})\\&=\sum_{m=1}^{M}\sum_{n=1}^{N}\mathrm{Var}(X_{mn})\\&+\sum_{m_1\neq m_2}\sum_{n_1\neq n_2}\mathrm{Cov}(X_{m_1n_1},X_{m_2n_2}),\end{aligned} \tag{B3}$$

where Cov() denotes covariance. Since each of the random quantities $\xi(m,n)$ is uncorrelated, the variance in (B3) is reduced as

$$\mathrm{Var}\left(\sum_{m=1}^{M}\sum_{n=1}^{N}X_{mn}\right)=\sum_{m=1}^{M}\sum_{n=1}^{N}\mathrm{Var}(A'_{mn}\left|b_{mn}\right|\cos\xi\left(m,n\right)). \tag{B4}$$

According to the properties of variance, (B4) is transformed as

$$\begin{aligned}&\mathrm{Var}\left(\sum_{m=1}^{M}\sum_{n=1}^{N}X_{mn}\right)\\&=\sum_{m=1}^{M}\sum_{n=1}^{N}(A'_{mn})^2\left|b_{mn}\right|^2\mathrm{Var}(\cos\xi\left(m,n\right)).\end{aligned} \tag{B5}$$

It can be found that $|b_{mn}|^2$ is always equal to 1. Thus, (B5) is transformed as

$$\begin{aligned}&\mathrm{Var}\left(\sum_{m=1}^{M}\sum_{n=1}^{N}X_{mn}\right)\\&=(A'_{mn})^2\sum_{m=1}^{M}\sum_{n=1}^{N}\mathrm{Var}(\cos\xi(m,n))\\&=\sum_{m=1}^{M}\sum_{n=1}^{N}(A'_{mn})^2\overline{\cos^2\xi\left(m,n\right)}\\&-\sum_{m=1}^{M}\sum_{n=1}^{N}(A'_{mn})^2\{\overline{\cos\xi(m,n)}\}^2,\end{aligned} \tag{B6}$$

which is (19) in the main text.

REFERENCES

[1] Zhou, H.-J., Y.-H. Huang, B.-H. Sun, and Q.-Z. Liu, "Design and realization of a flat-top shaped-beam antenna array," *Progress In Electromagnetics Research Letters*, Vol. 5, 159–166, 2008.

[2] Singh, A. K., M. P. Abegaonkar, and S. K. Koul, "Wide angle beam steerable high gain flat top beam antenna using graded index metasurface lens," *IEEE Transactions on Antennas and Propagation*, Vol. 67, No. 10, 6334–6343, 2019.

[3] Liu, C. and Y. Guo, "Flat-top line-shaped beam shaping and system design," *Sensors*, Vol. 22, No. 11, 4199, 2022.

[4] Kenane, E. H., F. Djahli, and A. Bartil, "Synthesis of cosecant linear antenna array pattern using a novel modified invasive weeds optimization," *Elektronika Ir Elektrotechnika*, Vol. 21, No. 5, 86–89, 2015.

[5] Chakraborty, A. and B. Das, "Scanning of sector and cosecant beams generated by a circular aperture," *IEEE Transactions on Antennas and Propagation*, Vol. 32, No. 9, 1000–1003, 2003.

[6] Baird, C. and G. Rassweiler, "Adaptive sidelobe nulling using digitally controlled phase-shifters," *IEEE Transactions on Antennas and Propagation*, Vol. 24, No. 5, 638–649, 2003.

[7] Steyskal, H., "Synthesis of antenna patterns with prescribed nulls," *IEEE Transactions on Antennas and Propagation*, Vol. 30, No. 2, 273–279, 2003.

[8] Steyskal, H., "Simple method for pattern nulling by phase perturbation," *IEEE Transactions on Antennas and Propagation*, Vol. 31, No. 1, 163–166, 2003.

[9] Zhang, Z.-Y., N.-W. Liu, S. Zuo, Y. Li, and G. Fu, "Wideband circularly polarised array antenna with flat-top beam pattern," *IET Microwaves, Antennas & Propagation*, Vol. 9, No. 8, 755–761, 2015.

[10] Khorasaninejad, M., W. T. Chen, R. C. Devlin, J. Oh, A. Y. Zhu, and F. Capasso, "Metalenses at visible wavelengths: Diffraction-limited focusing and subwavelength resolution imaging," *Science*, Vol. 352, No. 6290, 1190–1194, 2016.

[11] Aieta, F., M. A. Kats, P. Genevet, and F. Capasso, "Multiwavelength achromatic metasurfaces by dispersive phase compensation," *Science*, Vol. 347, No. 6228, 1342–1345, 2015.

[12] Cui, T. J., M. Q. Qi, X. Wan, J. Zhao, and Q. Cheng, "Coding metamaterials, digital metamaterials and programmable metamaterials," *Light: Science & Applications*, Vol. 3, No. 10, e218–e218, 2014.

[13] Bao, L., R. Y. Wu, X. Fu, Q. Ma, G. D. Bai, J. Mu, R. Jiang, and T. J. Cui, "Multi-beam forming and controls by metasurface with phase and amplitude modulations," *IEEE Transactions on Antennas and Propagation*, Vol. 67, No. 10, 6680–6685, 2019.

[14] Liang, J. C., L. Zhang, Z. Luo, R. Z. Jiang, Z. W. Cheng, S. R. Wang, M. K. Sun, S. Jin, Q. Cheng, and T. J. Cui, "A filtering reconfigurable intelligent surface for interference-free wireless communications," *Nature Communications*, Vol. 15, No. 1, 3838, 2024.

[15] Chen, J., W. Li, K. Gong, X. Lu, M. S. Tong, X. Wang, and G.-M. Yang, "Gesture-controlled reconfigurable metasurface system based on surface electromyography for real-time electromagnetic wave manipulation," *Nanophotonics*, Vol. 14, No. 1, 107–119, 2025.

[16] Li, Q., C. Wu, Z. Zhang, S. Zhao, B. Zhong, S. Li, H. Li, and L. Jin, "High-purity multi-mode vortex beam generation with full complex-amplitude-controllable metasurface," *IEEE Transactions on Antennas and Propagation*, Vol. 71, No. 1, 774–782, 2022.

[17] Xu, H., J. W. Wu, Z. X. Wang, R. W. Shao, H. Q. Yang, and T. J. Cui, "Two-dimensional and high-order directional information modulations for secure communications based on programmable metasurface," *Nature Communications*, Vol. 15, No. 1, 6140, 2024.

[18] Shao, R. W., J. W. Wu, J. Li, S. Meng, Y. Xu, Z. X. Wang, W. Tang, Q. Cheng, S. Jin, and T. J. Cui, "Dual-channel near-field holographic mimo communications based on programmable digital coding metasurface and electromagnetic theory," *Nature Communications*, Vol. 16, No. 1, 915, 2025.

[19] Yang, J., Y. Li, J. W. Wu, J. Y. Dai, S. R. Wang, H. D. Li, Y. J. Chen, and Q. Cheng, "Transmission-reflection-integrated programmable metasurface for simultaneous and independent control of bidirectional incident waves," *Advanced Functional Materials*, Vol. 35, No. 20, 2419681, 2025.

[20] Jiang, M., W. J. Ran, J. W. Wu, X. Yang, Y. Li, R. Y. Wu, Q. Cheng, J. Hu, and T. J. Cui, "Efficient and accurate simulations of metamaterials based on domain decomposition and unit feature database," *IEEE Transactions on Antennas and Propagation*, Vol. 72, No. 11, 8635–8646, 2024.

[21] Feng, R., B. Ratni, J. Yi, H. Zhang, A. de Lustrac, and S. N. Burokur, "Versatile metasurface platform for electromagnetic wave tailoring," *Photonics Research*, Vol. 9, No. 9, 1650–1659, 2021.

[22] Feng, R., B. Ratni, J. Yi, Z. Jiang, H. Zhang, A. de Lustrac, and S. N. Burokur, "Flexible manipulation of bessel-like beams with a reconfigurable metasurface," *Advanced Optical Materials*, Vol. 8, No. 23, 2001084, 2020.

[23] Wu, J. W., Z. X. Wang, R. Y. Wu, H. Xu, Q. Cheng, and T. J. Cui, "Simple and comprehensive strategy to synthesize huygens metasurface antenna and verification," *IEEE Transactions on Antennas and Propagation*, Vol. 71, No. 8, 6652–6666, 2023.

[24] Wu, J., Q. Hua, H. Xu, H. Yang, Z. Wang, Q. Cheng, and T. J. Cui, "Realizing complex beams via amplitude-phase digital coding metasurfaces and semidefinite relaxation optimization," *Frontiers of Information Technology & Electronic Engineering*, Vol. 24, No. 12, 1708–1716, 2023.

[25] Keizer, W. P. M. N., "Fast low-sidelobe synthesis for large planar array antennas utilizing successive fast fourier transforms of the array factor," *IEEE Transactions on Antennas and Propagation*, Vol. 55, No. 3, 715–722, 2007.

[26] Balanis, C. A., *Modern Antenna Handbook*, John Wiley & Sons, 2011.

[27] Ding, X., Z. Wang, G. Hu, J. Liu, K. Zhang, H. Li, B. Ratni, S. N. Burokur, Q. Wu, J. Tan, and C.-W. Qiu, "Metasurface holographic image projection based on mathematical properties of fourier transform," *Photonix*, Vol. 1, No. 1, 16, 2020.

[28] Li, J., F. Zhang, M. Pu, Y. Guo, X. Li, X. Ma, C. Wang, and X. Luo, "Quasi-continuous metasurface beam splitters enabled by vector iterative fourier transform algorithm," *Materials*, Vol. 14, No. 4, 1022, 2021.

[29] Schelkunoff, S. A., "A mathematical theory of linear arrays," *The Bell System Technical Journal*, Vol. 22, No. 1, 80–107, 1943.

[30] Recioui, A. and A. Azrar, "Use of genetic algorithms in linear and planar antenna array synthesis based on schelkunoff method," *Microwave and Optical Technology Letters*, Vol. 49, No. 7, 1619–1623, 2007.

[31] Woodward, P. M., "A method of calculating the field over a plane aperture required to produce a given polar diagram," *Journal of The Institution of Electrical Engineers — Part IIIA: Radiolocation*, Vol. 93, No. 10, 1554–1558, 1946.

[32] Woodward, P. M. and J. D. Lawson, "The theoretical precision with which an arbitrary radiation-pattern may be obtained from a source of finite size," *Journal of The Institution of Electrical Engineers — Part III: Radio and Communication Engineering*, Vol. 95, No. 37, 363–370, 1948.

[33] Takabayashi, N., K. Kawai, M. Mase, N. Shinohara, and T. Mitani, "Large-scale sequentially-fed array antenna radiating flat-top beam for microwave power transmission to drones," *IEEE Journal of Microwaves*, Vol. 2, No. 2, 297–306, 2022.

[34] Zhang, H., T. Lan, S. Zhao, Q. He, and Z. Li, "Flat-topped beams using phase compensation based on low-profile transmitarray," *Applied Computational Electromagnetics Society Journal (ACES)*, Vol. 38, No. 6, 409–415, 2023.

[35] Dorigo, M., M. Birattari, and T. Stutzle, "Ant colony optimization," *IEEE Computational Intelligence Magazine*, Vol. 1, No. 4, 28–39, 2007.

[36] Zhu, D. Z., E. B. Whiting, S. D. Campbell, D. B. Burckel, and D. H. Werner, "Optimal high efficiency 3D plasmonic metasurface elements revealed by lazy ants," *Acs Photonics*, Vol. 6, No. 11, 2741–2748, 2019.

[37] Bertsimas, D. and J. Tsitsiklis, "Simulated annealing," *Statistical Science*, Vol. 8, No. 1, 10–15, 1993.

[38] Zhao, Y., X. Cao, J. Gao, Y. Sun, H. Yang, X. Liu, Y. Zhou, T. Han, and W. Chen, "Broadband diffusion metasurface based on a single anisotropic element and optimized by the simulated annealing algorithm," *Scientific Reports*, Vol. 6, No. 1, 23896, 2016.

[39] Li, X. M., X. Xi, J. Chen, H. B. Wu, X. Li, Q. Chen, and R.-X. Wu, "Stereo meta-atom enabled phase-amplitude gradient metasurface for circularly polarized waves," *Advanced Optical Materials*, Vol. 10, No. 13, 2200326, 2022.

[40] Villegas, F. J., "Parallel genetic-algorithm optimization of shaped beam coverage areas using planar 2-D phased arrays," *IEEE Transactions on Antennas and Propagation*, Vol. 55, No. 6, 1745–1753, 2007.

[41] Li, H., G. Wang, T. Cai, H. Hou, and W. Guo, "Wideband transparent beam-forming metadevice with amplitude-and phase-controlled metasurface," *Physical Review Applied*, Vol. 11, No. 1, 014043, 2019.

[42] Slowik, A. and H. Kwasnicka, "Evolutionary algorithms and their applications to engineering problems," *Neural Computing and Applications*, Vol. 32, No. 16, 12 363–12 379, 2020.

[43] Clemente, A., L. Dussopt, R. Sauleau, P. Potier, and P. Pouliguen, "Wideband 400-element electronically reconfigurable transmitarray in X band," *IEEE Transactions on Antennas and Propagation*, Vol. 61, No. 10, 5017–5027, 2013.

[44] Jafar-Zanjani, S., S. Inampudi, and H. Mosallaei, "Adaptive genetic algorithm for optical metasurfaces design," *Scientific Reports*, Vol. 8, No. 1, 11040, 2018.

[45] Lalbakhsh, A., M. U. Afzal, and K. P. Esselle, "Multiobjective particle swarm optimization to design a time-delay equalizer metasurface for an electromagnetic band-gap resonator antenna," *IEEE Antennas and Wireless Propagation Letters*, Vol. 16, 912–915, 2017.

[46] Smith, M. and Y. Guo, "A comparison of methods for randomizing phase quantization errors in phased arrays," *IEEE Transactions on Antennas and Propagation*, Vol. 31, No. 6, 821–828, 1983.

[47] Aronov, F. A., "New method of phasing for phased array using digital phase shifters," *Radio Engineering and Electronic Physics*, Vol. 11, 1035–1040, 1966.

[48] Jiang, W., Y. Guo, T. Liu, W. Shen, and W. Cao, "Comparison of random phasing methods for reducing beam pointing errors in phased array," *IEEE Transactions on Antennas and Propagation*, Vol. 51, No. 4, 782–787, 2003.

[49] Kashin, V. A., "Statistical synthesis of antenna arrays," *Radio Engineering and Electronic Physics*, Vol. 16, No. 11, 1851–1858, 1971.

[50] Steyskal, H., R. A. Shore, and R. Haupt, "Methods for null control and their effects on the radiation pattern," *IEEE Transactions on Antennas and Propagation*, Vol. 34, No. 3, 404–409, 1986.

[51] Wang, Z. X., H. Q. Yang, F. Zhai, J. W. Wu, Q. Cheng, and T. J. Cui, "A low-cost and low-profile electronically programmable bit array antenna for two-dimensional wide-angle beam steering," *IEEE Transactions on Antennas and Propagation*, Vol. 71, No. 1, 342–352, 2023.